

Mechanics of vibrotactile sensors for applications in skin-interfaced haptic systems



Jin-Tae Kim^{a,1}, Hee-Sup Shin^{a,1}, Jae-Young Yoo^{a,1}, Raudel Avila^{a,1}, Yonggang Huang^b, Yei Hwan Jung^{c,*}, J. Edward Colgate^{b,*}, John A. Rogers^{a,*}

^a Querrey Simpson Institute for Bioelectronics, Northwestern University, Evanston, IL 60208, USA

^b Department of Mechanical Engineering, Northwestern University, Evanston, IL 60208, USA

^c Department of Electronic Engineering, Hanyang University, Seoul, Republic of Korea

ARTICLE INFO

Article history:

Received 1 October 2022

Received in revised form 24 November 2022

Accepted 26 November 2022

Available online 5 December 2022

Keywords:

Haptics

Actuators

Perception

3D digital image correlation

ABSTRACT

Recent advances in haptic interfaces support a range of options in adding sensations of touch to virtual and augmented reality experiences. A fundamental understanding of the mechanics associated with coupling between vibro-tactile actuators and the skin is important in considering device designs and interpreting sensory perceptions. Here, we investigate vibrational dynamics induced by the three main classes of such actuators in bilayer elastomer structures that capture essential mechanical properties of human skin. The measurements rely on three dimensional digital image correlation methods, with corresponding simulations based on finite element analysis techniques. Studies examine the effects of key parameters relevant to the mechanics and resulting sensations, such as those related to contact area, actuation amplitude and spatio-temporal distributions of displacements in terms of both surface and body waves. Results reveal that tactor type actuators operate in a power efficient mode to produce deformations largely oriented out of the plane of the skin, for robust sensations that can, however, depend strongly on mounting strategy. Actuators based on eccentric rotating motors yield deformations with similar magnitudes but with substantial in-plane components and reduced sensations. Key attractive features of these actuators are in small, lightweight designs that facilitate mounting on the skin and deployment into large arrays. A third type of device, linear resonant actuators, produce the weakest sensations and the lowest power efficiencies, with limited potential for practical applications.

© 2022 Elsevier Ltd. All rights reserved.

1. Introduction

Vibration-based tactile displays offer various effective forms of information transfer through the skin [1]. Actuators for such purposes span those that rely on electromagnetic, electrostatic, piezoelectric and pneumatic components to those that exploit shape memory alloys [1,2]. Electromagnetic actuators are particularly attractive [3–6] due to their versatility in operating modality, simplicity in construction and convenience in use. Eccentric rotating mass (ERM) actuators and linear electromagnetic actuators are the two most common options. Devices of the former type use a direct current (DC) motor with an off-center mass adhered to the output shaft, all encased in a metal housing. Activation leads to large angular motions induced by centrifugal forces that follow from the rotation of the mass. On the skin, the result is a three-dimensional motion dynamics that resembles that of a Euler's

disk [3,7], with vibrations that occur both in and out of the plane of the skin [8]. Although the forces generated by an ERM actuator can be significant, a disadvantage is that the torque and speed are coupled, such that the vibration amplitude and frequency cannot be controlled independently [7].

By comparison to ERM actuators, linear electromagnetic actuators offer a simple operating mechanism, based on voice coils and magnets suspended on springs. Similar to loudspeakers, harmonic motions of the magnet/spring follow from electromagnetic forces generated by passage of alternating current through the coil. Resulting vibrations occur linearly in a direction normal to the surface of the skin. Such actuators are available in two types, linear resonant actuators (LRAs) and vibrotactile linear actuators (e.g. tactors). For the former, the entire housing of the actuator interacts with the skin, as with an ERM device. The housing for the latter serves as a surrounding frame that restricts interaction with the skin through a comparatively small contactor. These different designs and interactions with the skin lead to distinct dynamics [7,9]. Unlike ERM actuators, LRAs and tactors operate on AC current, with independent control over the both amplitude and frequency within a certain resonance bandwidth [2].

* Corresponding authors.

E-mail addresses: yjung@hanyang.ac.kr (Y.H. Jung), colgate@northwestern.edu (J.E. Colgate), jrogers@northwestern.edu (J.A. Rogers).

¹ These authors contributed equally to this work.

Tactile perception follows from the activity of low-threshold mechanoreceptors (LTMRs) that convert mechanical stimuli into action potentials in peripheral nerves [10]. Four distinct types of LTMRs exist in the skin at different depths, classified according to the rate of adaptation and size of response fields (Table S1). Comprehensive mechanical analyses of the coupling between these LTMRs and skin-interfaced vibrotactile actuators can serve as design guidelines at the component and system levels in haptic devices. Viscoelastic properties of the skin modify the characteristics of vibrotactile actuators by adding mechanical impedances such as restoring and damping forces. For example, additional impedances with ERM actuators increase their torque and decrease their angular rotation rate and associated vibration frequency [7]. In this and other contexts, the methods for mounting the actuators onto the skin are critically important. For linear electromagnetic actuators, a surrounding frame can alter the inertial reference and contact area [7,11–13]. Previously reported studies of actuators on the skin [7,9,14] focus on psychophysical measurements of perceptual intensity or spatial acuity [8,11,15,16] and tactile icons [17–19]. Some investigations emphasize quantitative characterization of motions of the skin induced by vibrotactile actuators associated with tactile perception using accelerometers [20,21]. Means by which stresses generated by the actuators propagate through the depths of various layers of skin remain unclear [10].

The work presented here explores three-dimensional, spatio-temporal distributions of strain induced in skin phantoms both on their surfaces and into their depths by ERM actuators, LRAs and tactors using three-dimensional digital image correlation (3D-DIC) techniques and finite element analysis (FEA) methods. Investigations across different contact areas and at various depths relevant to the locations of mechanoreceptors with extensive perception tests provide insights into neurophysiological and psychophysical aspects. The following sections describe the types of vibrotactile actuators and experimental setups (2.1), the mechanics of ERM (2.2) and tactor (2.3) actuators, the strain responses in skin phantoms (2.4), the corresponding FEA results (2.5) and the findings from perception studies (2.6).

2. Results and discussions

2.1. Vibrotactile sensors and experimental setup

Fig. 1a shows photographs of commonly used vibrotactile actuators for haptic devices, including the ERM (Precision Microdrives™ model No. 910-108.002 with the weight of 1.29 g and outer diameter of 10 mm), LRA (Precision Microdrives™ model No. C10-100 with the weight of 1.37 g and outer diameter of 10 mm) and tactor (ATAC Tactor; weight = 34.72 g; outer diameter = 30 mm) all designed with the same diameter of contact with the skin, $L_0 = 1$ cm. As described in the introduction, these actuators incorporate similar electromagnetic forces, to either spin a mass (ERM) or to push up and down a mass without a surrounding support structure (LRA) or with such a structure (tactor). Fig. 1b and Fig. S1 show photographs of additional components that allow various diameters of contact, L , with the skin and skin phantoms. For a balanced comparison among these actuators, the studies involve a fixed operating power (in the range of 100 mW) (Fig. S2) determined by multiplying the supply voltage (DC value for the ERM actuator; and root mean square (RMS) value for the LRA and tactor) and the calculated RMS current. Details of the power analyses can be found in the Methods section.

Fig. 1d presents a schematic illustration of mechanoreceptors and their distribution through the layers of the skin. Controlled studies use phantom skin structures that offer (i) moduli and bilayer structures that resemble human skin and (ii) optical transparency with embedded speckle patterns at two different depths.

Fig. 1e and Fig. S3 illustrate such a phantom made using pieces of polydimethylsiloxane (PDMS) formed with different thicknesses ($h_0 = 13$ mm; $h_2 = 2$ mm) and moduli ($E_1 = 419 \pm 0.9$ kPa; $E_2 = 68 \pm 1.3$ kPa). The depths of the speckle patterns correspond to $h_1 = 200$ μ m and $h_2 = 2$ mm, as the approximate boundaries from the epidermis to dermis and dermis to hypodermis, respectively [22]. LTMRs with Meissner corpuscles and Merkel discs reside near h_1 ; those with Pacinian and Ruffini corpuscles are close to h_2 (Table S1).

3D displacements and strains induced by actuators with various L at h_1 and h_2 follow from measurements based on 3D-DIC (Fig. 1e) [23]. Fig. 1f and Supplementary video 1 show the maximum displacement magnitudes $\|X\|$ induced by each actuator at a fixed power of ~ 120 mW. For these commercially available devices, the values of $\|X\|$ for the LRA are significantly smaller than those of other actuators, consistent with previously reported findings [3]. The following studies focus, therefore, only on the ERM actuator and tactor. The color range of the plots for the ERM actuators is only half of that for tactors, as the former and latter vibrate from peak to peak and zero to peak, respectively, with respect to the initial state of the skin deformation.

2.2. Mechanics of ERM actuators

The coupled dynamics that exist between an ERM actuator and the skin lead to complex, large-amplitude motions and corresponding sensory perceptions that are stronger than those associated with LRA and other voice-coil-type actuators, excluding the tactor [3]. Quantitative studies of the mechanisms for interfacing with viscoelastic materials as a function of depths relevant to the locations of mechanoreceptors are essential to decipher the key parameters that govern tactile sensations. The 3D-DIC measurements consist of an ERM actuator operated at a fixed power, 120 mW, with three different contact areas, $L/L_0 = 1/2, 3/4$ and 1 at two depths, $h_1 = 0.2$ mm and $h_2 = 2$ mm. Fig. 2a and Supplementary Video 2 show displacements near the surface, h_1 , during a representative instant of the ERM actuator operation. The dominant displacements lie along the x and y axes. Significant out-of-plane displacements, Δz , also occur, with opposite directions at the opposing edges of the ERM actuator. The out-of-plane displacements are elongated along the binormal direction of the ERM actuator displacement vector, indicated as arrows in Fig. 2a and b. Displacements occur mainly in the vicinity of the actuator, particularly for the out-of-plane direction. Fig. 2b and Supplementary Video 3 show displacements evaluated at h_2 . The in-plane displacements, Δx and Δy appear inverted relative to those at h_1 , with two peaks near the edges of the contact area. At a representative instant, values for Δy include both positive and negative displacements in each quadrant, consistent with the Poisson effect. These results reveal that the in-plane displacements propagate into the depth as shown in Fig. 2c. As L/L_0 decreases, the rotational motion promotes a large amplitude in the oscillation of the actuator due to a similar degree of force applied to a small area. The data indicate a coupling effect between the amplitude and frequency of vibration, as shown in the time dependent, in-plane displacement profiles at the center of the actuator (Fig. 2d). As L/L_0 decreases, the amplitude decreases and frequency increases, thereby affecting the dependence of the acceleration profiles on L/L_0 (Fig. S4a). The shear wave velocity, c , evaluated for the case with $L/L_0 = 0$ at h_1 is 8.25 ± 0.5 m/s (Fig. 2e). The analytic equation for the shear velocity in a linear elastic solid is $c = \sqrt{E/2(1+\nu)}\rho$, where $\nu = 0.5$ is Poisson's ratio and $\rho = 965$ kg/m³ is the density of the artificial skin, providing a reasonable approximation to the experimental values [24]. By taking $E_1 = 68$ kPa as a lower bound and $E_2 = 419$ kPa as the upper bound for the phantom skin

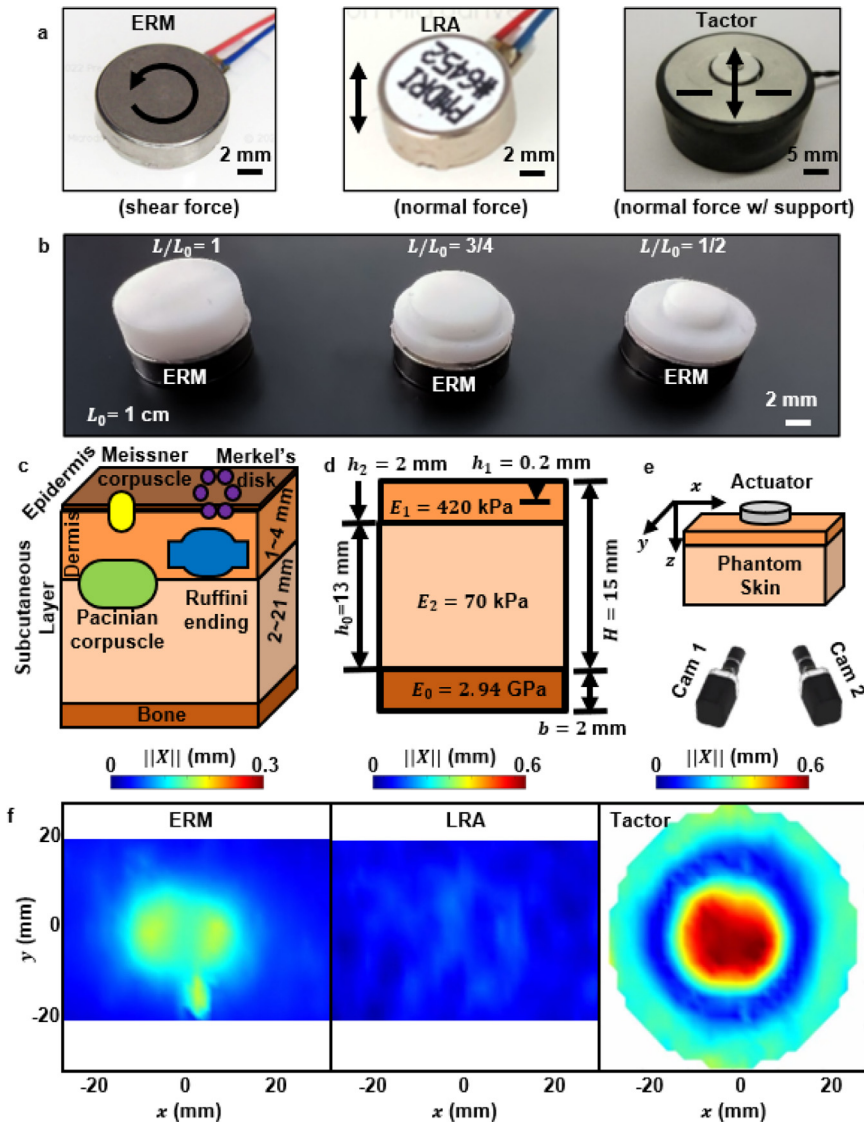


Fig. 1. Vibrotactile actuators, experimental setups and representative measurement results. (a) photographs of ERM, LRA and tactor actuators with identical contact diameters $L_0 = 1$ cm (b) 3D printed parts that mount on top of ERM actuators to realize different contact diameters, L . Schematic illustrations of (c) mechanoreceptors and their locations within the depth of the skin, (d) design of a bilayer skin phantom, (e) 3D-DIC experiment setup. (f) Measured displacement magnitudes ($\|X\|$) associated with ERM, LRA and tactor actuators at the surface of the skin phantom, each operated at a power of 120 mW.

elastic modulus, we obtain a range between 4.9 m/s and 12 m/s for the shear wave velocity. Then, the range of Rayleigh wave speed at the surface of the phantom skin can be approximated as $c_R = c [0.875 - 0.2v - 0.05(v + 0.25)^3]$ giving values between 3.7 m/s and 9 m/s. In the context of this work, the strain levels at both the phantom skin surface and at depths at h_1 and h_2 over the region of interest (area of 400 mm²) remain small $\|\epsilon\| \leq 0.04$. Also, the deformation at the phantom skin surface and in deep tissue are small as compared to the characteristic lengths of the devices and we assume that the tissue does not have time to relax due to the speed of the actuators and strain level. Profiles of Δx along the center line tangent to the displacement vector of the ERM actuator provide further indication that in-plane deformations transmit diagonally along the depth (Fig. 2f).

2.3. Mechanics of tactor actuators

The support structure of the tactor, which surrounds the vibrating unit, responds to the reaction force induced by operation of the actuator. As a result, the tactor transmits vibrational motions straight down into the depth of the skin (Supplementary

Video 4). To allow fair comparisons to the results from the ERM actuators, the measurements involve (i) operation at a resonant frequency of 125 Hz, (ii) attachment of the vibrating unit to the skin phantom with double sided tape, (iii) fixation of the outer edge of the support structure (thickness of 5 mm, Fig. S1) to the skin phantom to minimize inconsistencies associated with boundary conditions. As expected, the displacements occur mainly in the out of plane direction, along the z axis, with associated in plane displacements in opposite directions along the x and y axes, as shown in Fig. 3a and Supplementary Video 5. The overall amplitudes are similar to those induced by the ERM actuator. The directions and magnitudes of the paired in-plane displacements change sign and increase, while those out of plane decrease, with depth, h_2 regardless of L/L_0 (Fig. 3b and Supplementary Video 6). Results of change in the direction of in-plane displacements indicate the presence of a body wave along the depth as described in Fig. 3c. Unlike the case of an ERM actuator, the in-plane displacements increase at the interface of h_2 due to the change of materials modulus at the location. The value of L/L_0 strongly influences the out of plane displacement, Δz , at the center of the actuator with respect to time, as shown

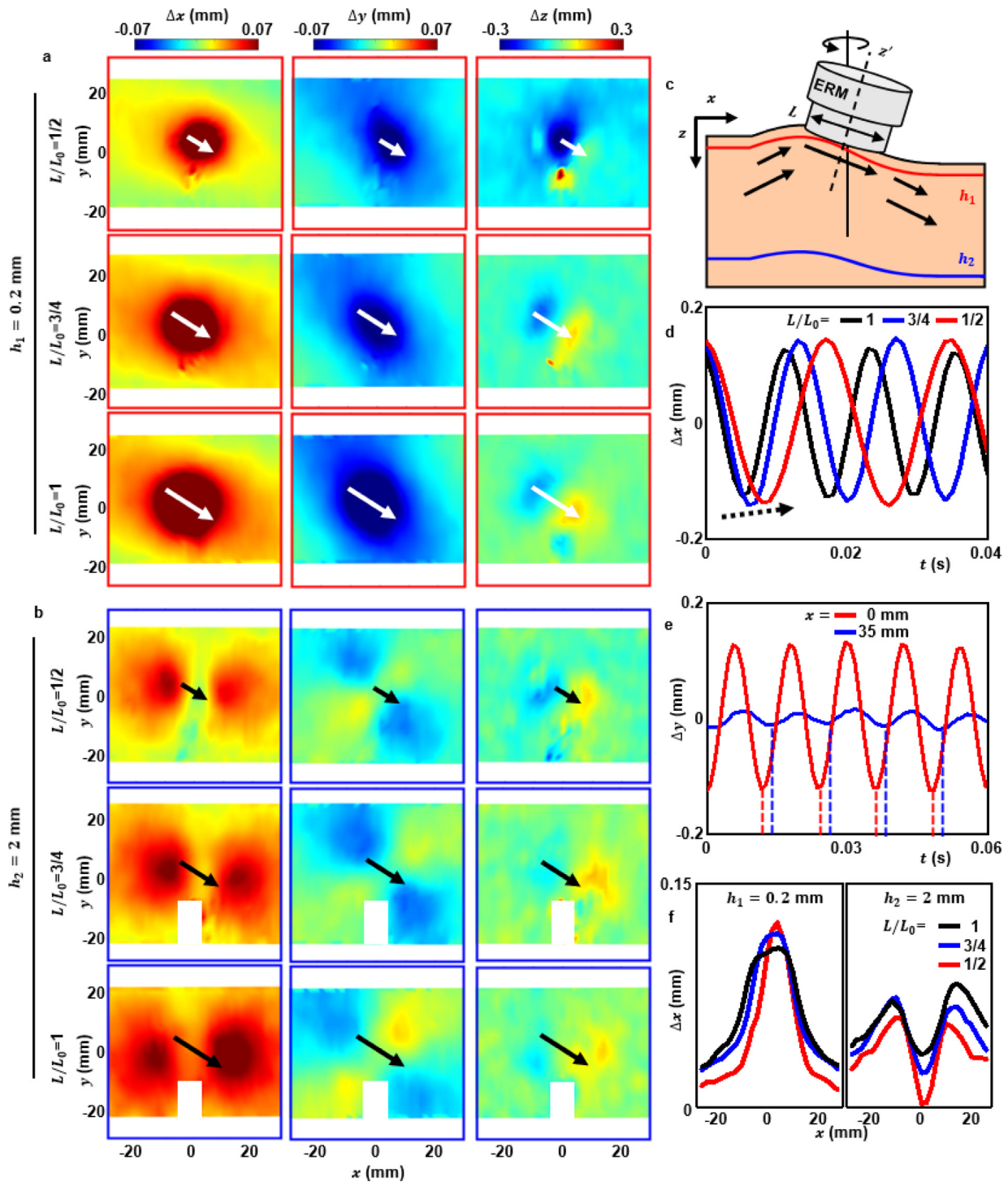


Fig. 2. Spatio-temporal characteristics of strains induced in a skin phantom created by operation of an ERM actuator evaluated by 3D-DIC. Instantaneous displacements along x (Δx), y (Δy) and z (Δz) with $L/L_0 = 1, 3/4, 1/2$ at depths of (a) 0.2 mm, h_1 and (b) 2 mm, h_2 . The omitted white sections of the data represent optical noise induced by oscillating electrical wires of the ERM actuator. (c) Free-body diagram of an ERM actuator on a sample of phantom skin. (d) in-plane displacement, Δx , as a function of time at the center of the ERM actuator at a depth of h_1 . (e) in-plane displacement, Δy , as a function of time at the center, $x = 0$, and $x = 35$ mm for the case of $L/L_0 = 1$. Dotted lines denote the instants when the peak displacements occur. (f) center line profiles of Δx when the maximum displacements occur at (left) h_1 and (right) h_2 .

in Fig. 3d and e. Specifically, Δz varies inversely with L/L_0 , but the frequency is independent to L/L_0 , as expected (Fig. S4b). The acceleration induced by the tactor is much greater than that of the ERM actuator, for these commercial components. Another key

difference is that the support structure of the tactor mitigates lateral wave propagation (Fig. 3e). The effect may be to spatially isolate the sensory perception. Profiles of Δz along the centerline further clarify the nature of the motions (Fig. 3f).

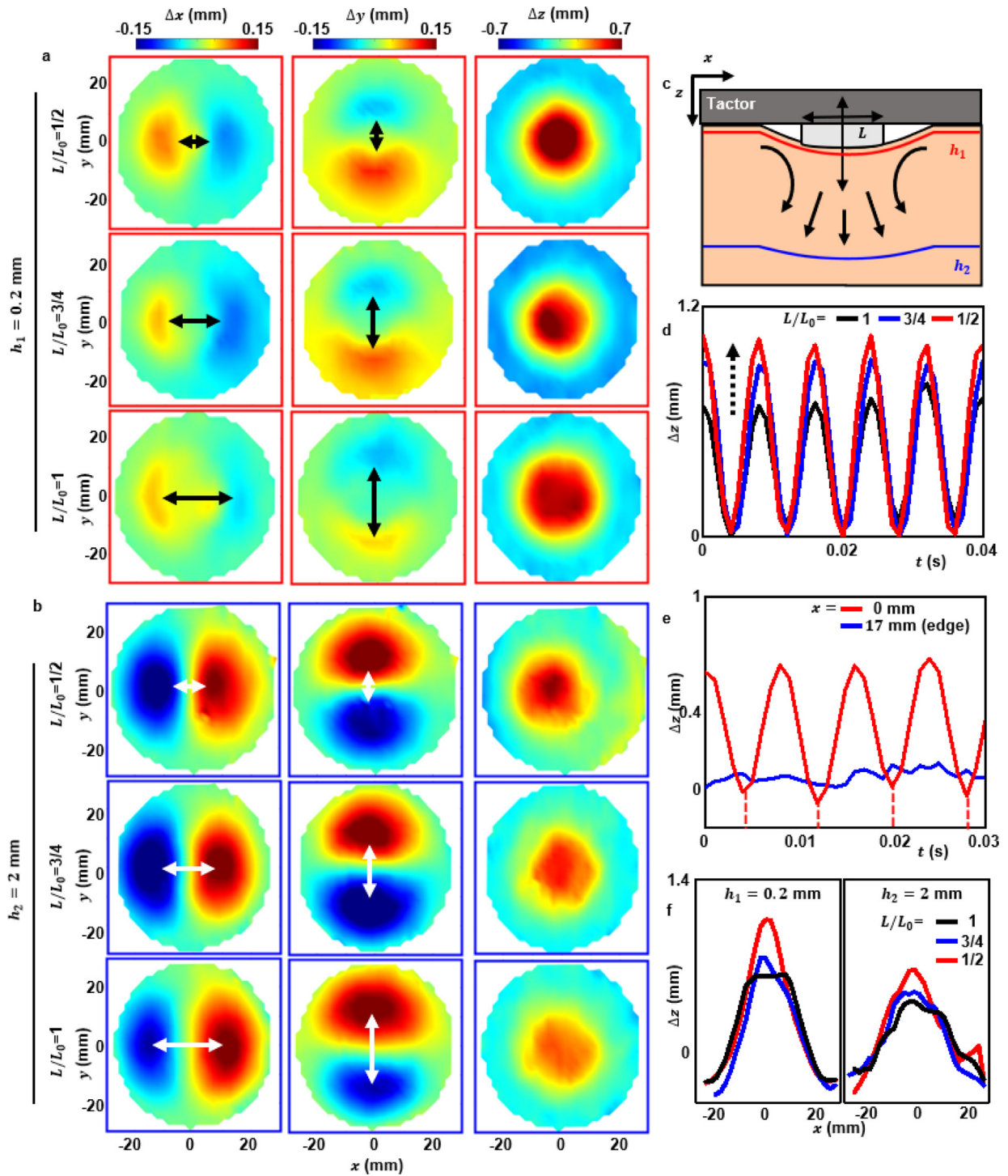


Fig. 3. Spatio-temporal characteristics of strains induced in a skin phantom created by operation of a tactor evaluated by 3D-DIC. Instantaneous displacements along x (Δx), y (Δy) and z (Δz) with $L/L_0 = 1, 3/4, 1/2$ at depths of (a) 0.2 mm, h_1 and (b) 2 mm, h_2 . (c) Free-body diagram of a tactor actuator on a sample of phantom skin. (d) out-of-plane displacement, Δz , as a function of time at the center of the tactor at a depth of h_1 . (e) out-of-plane displacement, Δz , as a function of time at the center, $x = 0$, and $x = 17$ mm for the case of $L/L_0 = 1$. The dotted line denotes the instant when the peak displacements occur. (f) center line profiles of Δz when the maximum displacements occur at (left) h_1 and (right) h_2 .

2.4. Strain characteristics of ERM and tactor actuators

Strain directly connects to perception because mechanoreceptors act effectively as strain gauge sensors. Experiments to accurately measure these strains resolve displacements over 700 grid points in the investigation volume at a sampling rate > 4 times higher than the highest vibration frequency observed in this work. The Triangular Cosserat Point Elements (TCPE) method

allows for efficient and accurate strain estimations based on these results. This technique obtains and separates the rigid body motion, using standard least-squares minimization methods, and the finite nonlinear strain field, by treating each tetrahedron as a Cosserat Point Element, with the same spatial resolution [25]. The strain results for each actuator at different depths reveal distinctive characteristics. Strain fields induced by an ERM actuator exhibit high magnitudes around the border of the actuator near

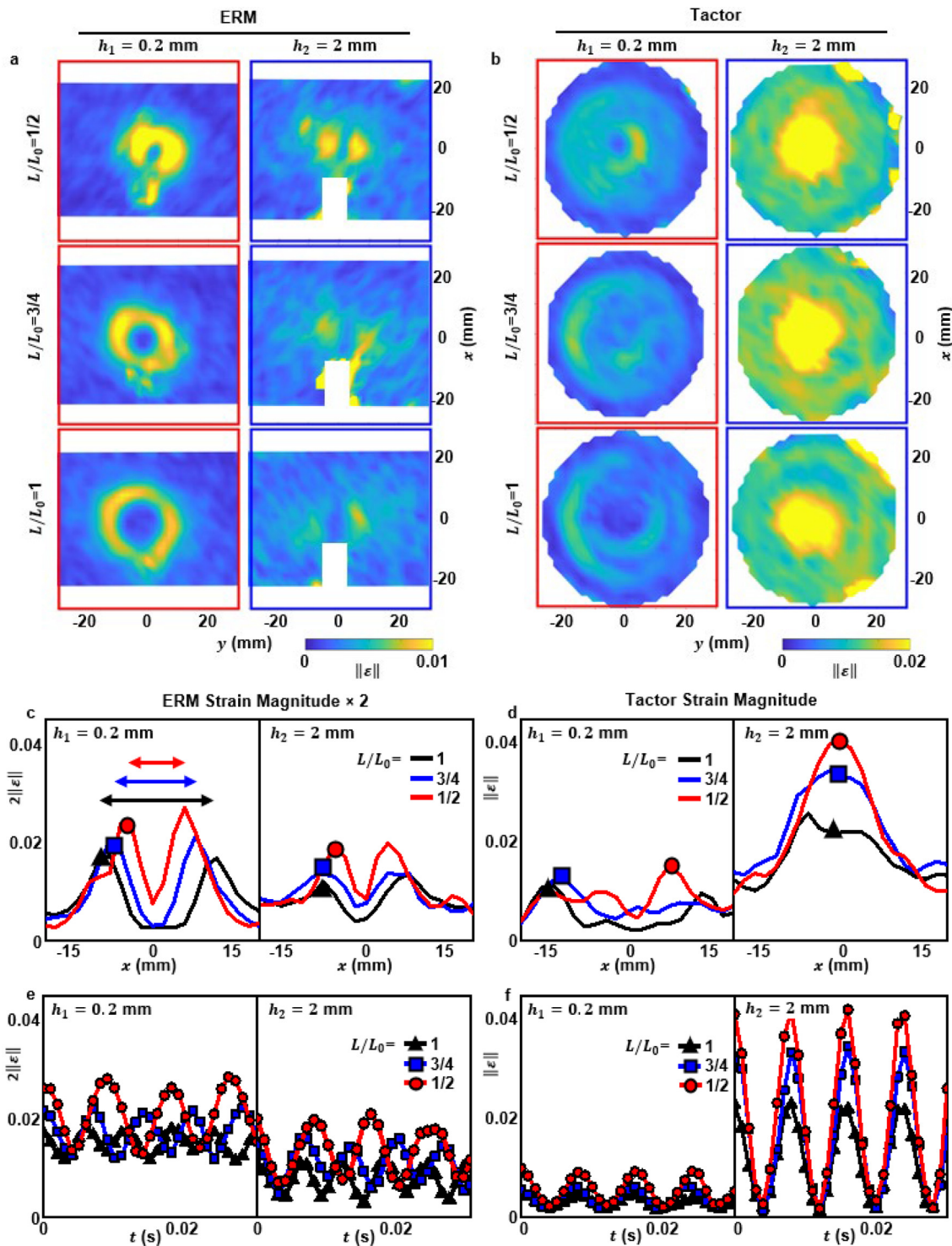


Fig. 4. Spatio-temporal characteristics of strains induced in a skin phantom created by operation of ERM actuator and tactor at similar power levels. Distribution of strain magnitude, $\|\epsilon\|$, at the instant where the maximum strain occurs for (a) an ERM actuator and (b) a tactor with $L/L_0 = 1, 3/4, 1/2$ at h_1 and h_2 . The omitted white sections of the data represent the optical noise induced by oscillating electrical wires of the ERM actuator. (c) center line profiles of $\|\epsilon\|$ when the maximum strain magnitudes occur at (left) h_1 and (right) h_2 for the (c) ERM actuator and (d) tactor. $\|\epsilon\|$ as a function of time at the local maxima at (left) h_1 and (right) h_2 for (e) ERM actuator and (f) tactor.

the surface of the skin. Those induced by the tactor reach maximum values at depths into the skin, following a parabolic profile (Fig. 4a and b; Supplementary Video 7 and 8). As mentioned previously, the color range for the plots of the strain field of the tactor is twice that for the ERM, as with the range for displacements, due to their peak-to-zero and peak-to-peak oscillations, respectively. Near the surface, h_1 , the peak strain by an ERM

actuator exceeds that from the tactor. By contrast, the peak strain induced by the tactor occurs at depth, h_2 , and exceeds the peak strain by an ERM actuator at h_1 (Fig. 4c, d). The magnitudes of the strains exhibit an inverse relationship to contact area, similar to the case of the displacements. Time profiles of these strain further provide insights into perception, as shown in Fig. 4e and f. The strain for the ERM near h_1 with $L/L_0 = 1/2$ in a temporal

domain exhibits the largest amplitude with respect to h and L/L_0 , similar to the characteristics of strain magnitude in the spatial domain. On the other hand, the frequency of oscillating strain changes over L/L_0 due to its naïve mechanism (Fig. 4e). This coupling between amplitude and frequency of vibration further affects corresponding values for strain rate. The amplitudes of strains induced by the tactor at h_2 are larger than those of the ERM actuator regardless of h and L , operating at a fixed frequency, as expected (Fig. 4f).

2.5. Computational modeling and simulation

These various effects can be captured using FEA. The focus is on instantaneous displacement and strain profiles for various L/L_0 and depths into the skin h , for comparison to 3D-DIC results. Further studies examine the effect of the modulus ratio E_1/E_2 (See Supplementary Data for details). The corresponding instantaneous displacements and strain magnitude contours are computed at time 10^{-1} s and plotted at $h = 10^{-1}$ mm and 10^{-2} mm as shown in Fig. 5a–d and Figs. S5–S7. For the ERM actuator, the simulations use an in-plane rotational force applied to the central axis of the actuator and out-of-plane forces at the opposite ends (Fig. 5a and b). For the tactor, a compressive pressure with a fixed sinusoidal frequency acts on the top surface of the actuator (Fig. 5c and d). The computed instantaneous displacements and strain magnitudes in Fig. 5a–b correlate to the in-plane and out of plane displacement and strain magnitude distributions for the ERM actuator experiments shown in Figs. 2a–b and 4a for the case when $L/L_0 = 3/4$. Similarly, Fig. 5c–d closely reproduces the experimental displacement and strain distribution shown in Figs. 3a–b and 4b for the tactor when $L/L_0 = 3/4$. For completion, the supplementary data in Fig. S5 and S6 shows the computed instantaneous displacements for all the cases $L/L_0 = 1/2, 3/4, 1$ that reproduce the experimental displacement distributions in Figs. 2a–b and 3a–b for the ERM actuator and tactor, respectively. The computed strain magnitudes for the cases $L/L_0 = 1/2, 3/4, 1$ are shown in Fig. S7 which correlate to the experimental results in Figs. 4a and 4b for the ERM actuator and Tactor, respectively.

Additional results reveal the effects of skin modulus in the amplitude and strain distribution, based on simulations that involve the modulus of the top layer from 50 kPa–500 kPa, corresponding to a ratio E_1/E_2 between 1–10, relevant to the range of skin properties [26], as shown in Fig. 5e–g. The computations yield the displacement amplitudes and strain magnitudes over a linear nodal path in the x -axis that intersects the actuator, normalized by values at $E_1/E_2 = 1$. Fig. 5e shows that the normalized in-plane amplitude for the ERM actuator and the normalized out-of-plane amplitude for the tactor both decrease with increasing E_1/E_2 . Specifically, relative to $E_1/E_2 = 1$, at $E_1/E_2 = 10$, the amplitudes produced by the ERM actuator and tactor reduce by 62% and 26%, respectively. These different trends are consistent with the surface and depth dominated interactions associated with the ERM actuator and tactor, respectively. Fig. 5f shows that increasing the modulus ratio by one order of magnitude to $E_1/E_2 = 10$, the amplitudes of motions induced by the ERM actuator decrease by approximately two orders of magnitude and those induced by the tactor decrease by approximately one order of magnitude as shown in Fig. 5g.

2.6. Perception studies

Blinded tests with 15 subjects (2 women, 13 men) ranging in age from 19 to 33 years (mean 29 years) reveal relationships between mechanical vibrations induced by these actuators and sensory perceptions. The studies use ERM actuator, LRA and tactor mounted on the lower arm, where the contact areas of the ERM

actuator and LRA attach onto the skin with a medical-grade adhesive (3M™ DC Medical High Adhesion Polyester Film Tape 1567). The vibrating unit and outer edge of tactor attach with the same adhesive. Here, a self-adherent wrap (3M™ Coban™ Self-Adherent Wrap 1583B) around entire actuator and lower arm minimizes inconsistencies in contact angle between the vibrating unit and the skin. Measurements of the perception intensity involve sweeping the operating powers of the actuators, each with contact diameters of 10 mm, 7.5 mm, and 5 mm, from 0.1 mW to 100 mW. The perception intensity associated with the tactor operating at 100 mW and with a contact area of $L/L_0 = 1$, defined as the reference tactor, is normalized to an intensity of 10. The reference tactor and other actuators with various L/L_0 mount on the right and left lower arms, respectively and operate alternatively for 5 s (Fig. S8). Participants compare the perceived vibration on the left arm to the one on the right arm. Overall, the observed intensities follow the strain characteristics observed by 3D-DIC, where the highest overall intensities arise from the tactor followed by the ERM actuator and then the LRA. The difference in intensities between tactor and ERM actuator have, remarkably, are similar to those of the peak strain magnitudes. As expected, the LRA exhibits the lowest intensities, with an average of < 1 at 100 mW. Reducing the contact area, over the range examined here, lead only to nominal increases in perception intensity.

Studies of the minimum operating power to produce a perceptible sensation, defined as the PMOP, for ERM actuator and tactor at various contact diameters (Fig. 6b and c) reveal the effects. The PMOP of ERM actuators with contact diameters of 10 mm, 7.5 mm and 5 mm are 14.7 mW (± 5.6 mW), 13.4 mW (± 3.5 mW), and 12.7 mW (± 4.8 mW), respectively (Fig. 6b). For the case of tactors, these values are 3 mW (± 1.1 mW), 2.4 mW (± 0.7 mW), and 2.0 mW (± 0.1 mW) (Fig. 6c), much smaller than those for the LRA and ERM actuator cases (Fig. 6d). This high level of power efficiency follows from two effects. First, the tactor maintains a constant operating frequency, at the resonant condition of 125 Hz, that is match to peak sensitivities of LTMRs (Table S1) across the full range of input powers. By contrast, the frequency of the ERM actuator decreases strongly with decreasing power (Fig. 5f). Second, the vibration mechanism of a tactor promotes maximum strain in deep tissues (Fig. 4b), coincident with the location of Pacinian corpuscles, which are primarily responsible for sensitivity to vibrations across large receptive fields and with fast adaptation.

At a power of 100 mW, the tactor with $L/L_0 = 1$ generates a perception intensity of 10; corresponding values for the ERM and LRA actuators with the same L/L_0 are 7.5 and 0.97, respectively (Fig. 6f). Direct comparisons of perception with respect to frequency and power between the ERM actuator and tactor involve mounting these actuators on the left and right lower arms, as before. Perceptual comparison questions use options that span “ERM strong – ERM slightly strong – similar vibration power – tactor slightly strong – tactor strong”. Investigations in this setup use various operating powers with and without matched operating frequencies (Fig. 6g–h). As the frequency of the ERM actuator changes with power (Fig. 6f), adjustments to the power supply for the tactor can be changed to match its operating frequency to that of the ERM actuator. In such cases, the perception intensity associated with the ERM actuator is larger than that for the tactor, partly due to operation of the latter outside of its resonance frequency range (Fig. 6g). On resonance, the tactor consistently produces stronger perception intensities than those with the ERM (Fig. 6h). Overall, in such cases the tactor requires a lower power to provoke a sensation, and produces a stronger perception than the ERM, with slight improvements as the contact area reduces. Drawbacks of commercially available versions of the tactor are in (i) its large size and high cost, (ii) narrow operating frequency

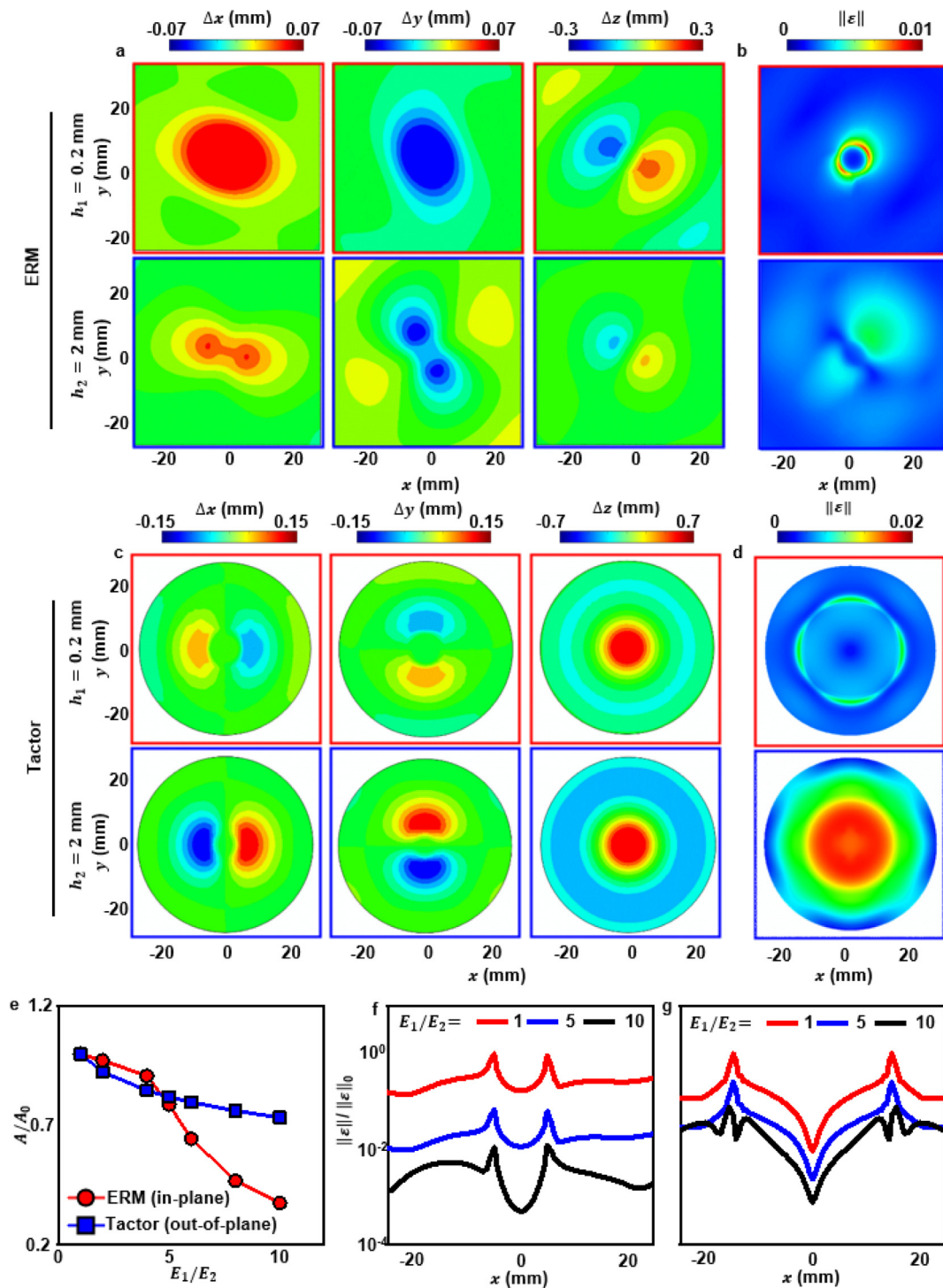


Fig. 5. Spatio-temporal characteristics of strains induced in a skin phantom created by operation of ERM and tactor actuators at identical power levels, as determined by finite element analysis. Distribution of (a) displacement and (b) strain magnitude induced by an ERM actuator at the instant where the maximum strain occurs. Distribution of (c) displacement and (d) strain magnitude induced by a tactor at the instant where the maximum strain occurs. In both cases, $L/L_0 = 3/4$ and the depths are $200 \mu\text{m}$ (red border), h_1 and 2 mm (blue border), h_2 . (e) Normalized amplitude of ERM actuator ($A_0 = 0.077$ mm; in-plane) and tactor ($A_0 = 0.83$ mm; out-of-plane) as a function of the ratio of the moduli of the upper and lower layers of the skin phantom, E_1/E_2 . Normalized distribution of strains for $E_1/E_2 = 1, 5, 10$ along the line ($x, y = 0$) at $z = 0.02$ mm for (f) ERM actuator and (g) tactor. (For interpretation of the references to color in this figure legend, the reader is referred to the web version of this article.)

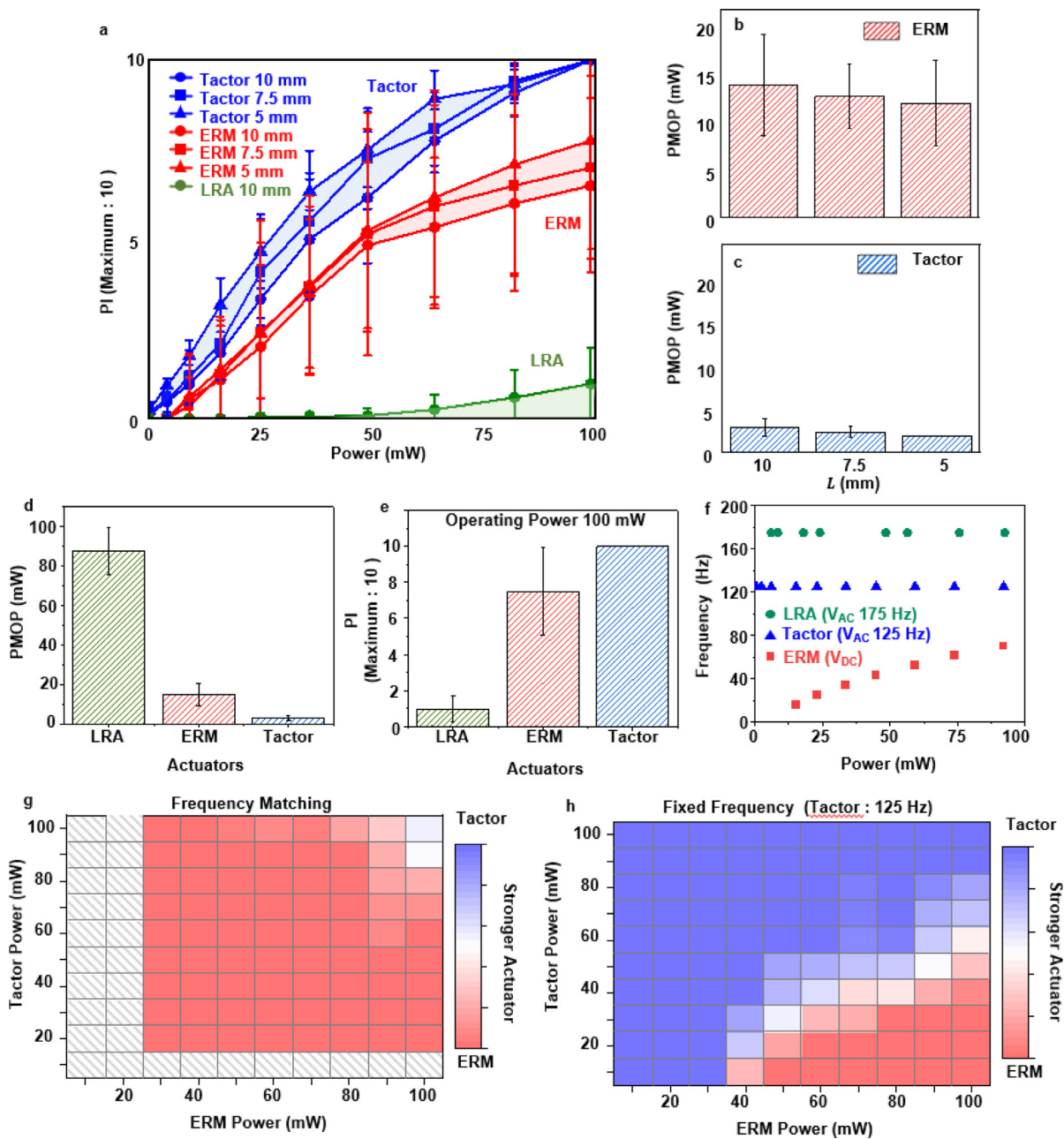


Fig. 6. Perception results of operation of the tactor, ERM, and LRA actuators on the lower arm (10 subjects). (a) Perceptual intensity (PI) as a function of operating power, where a value of 10 corresponds to the perception of a tactor actuator at 100 mW. (b–c) Perceptible minimum operating power (PMOP) of (b) ERM and (c) tactor actuators with contact diameters of 10 mm, 7.5 mm, and 5 mm. (d) PMOP values for actuators with contact diameters of 10 mm. (e) PI for operating powers of 100 mW. (f) Vibration frequency of tactor, ERM, and LRA actuators on the skin as a function of the operating power. (g) Perceptual comparisons between ERM actuator and tactor at the matched frequency based on the ERM’s frequency with respect to its power as shown in (f). (h) Perceptual comparisons between ERM actuator and tactor at a fixed frequency of 125 Hz (Resonance frequency of tactor).

range and (iii) rigid, planar construction and associated inconsistencies in mounting (Fig. S9). These features create difficulties for use of this technology in emerging classes of large-area, flexible haptic interfaces.

3. Conclusion

The presented work investigates mechanical vibrations induced by three commercially available, representative vibrotactile sensors used in recent haptic applications. Mechanical vibrations of a bilayer skin-like materials platform with various contact areas and along the depth, measured by 3D-DIC and validated by the FEA simulation, correlate with extensive perception

tests. The results show that the tactor triggers sensations and produces strong perceptions at low power, but with performance that depends strongly on mounting method. On the other hand, the ERM actuator yields a strong sensation, with an efficient mounting strategy and a comparatively small, lightweight form factor. This type of actuator suffers, however, from a coupling between amplitude and frequency and a dependence on its operating environments that follow from corresponding changes in inertia. The LRA is less suitable for haptic applications due to the relatively weak sensations that it produces. This work establishes a framework for comparison studies of performance related not only to actuator type but also actuator design features such as those related to coil geometries, magnet properties and overall

Table A.1
Measured passive component values and calculated parameters to estimate active power.

Actuator	Resistance (Ω)	Inductance (μH)	Impedance (Ω)	Phase angle (θ°)
LRA	27	415	27.003	0.854
C2 tactor	6	950	6.046	7.07

layouts. A combination of various types of actuators may ultimately be needed for robust, engaging haptic sensations through programmed engagement of different types of mechanoreceptors.

Declaration of competing interest

The authors declare that they have no known competing financial interests or personal relationships that could have appeared to influence the work reported in this paper.

Data availability

Data will be made available on request.

Acknowledgments

Y.H.J. acknowledges support from the National Research Foundation of Korea (NRF) grant funded by the Korean Government (MSIT) (no. 2022R1C1C1003994). R.A. acknowledges support from the NSF Graduate Research Fellowship (NSF Grant 1842165) and Ford Foundation Predoctoral Fellowship.

Appendix A. Method

A.1. Alternating current (AC) power analysis

The linear resonance actuator (LRA) and C2 tactor used AC current for their operation, as an equivalent circuit that consists of a resistor–inductor (RL) circuit in series. The impedance of this circuit is an important parameter in estimating the power consumption. Table A.1 shows the values of resistance and inductance for each actuator, measured using a commercial digital multimeter (115, FLUKE) and an LCR meter (E4980 A, Agilent). The impedance, Z , for an RL circuit is $Z = \sqrt{R^2 + X_L^2}$, where R , and X_L are the resistance and inductive reactance, respectively. The latter can be expressed as $X_L = 2\pi fL$ (f : the frequency of the AC current; L : inductance of the coil), evaluated at the resonance frequency for most cases reported here. The phase angle (θ) can be calculated using the relationship, $\theta(\text{radian}) = \cos^{-1}(R/Z)$, as summarized in Table A.1. In this RL circuit with single phase AC, the active power can be expressed as $P = V_{RMS}I_{RMS} \cos(\theta)$, where V and I are supplied voltage and current, respectively, and the subscript stands for their root mean square. Considering the estimated phase angles, the active power of both actuators can be approximated to $P = V_{RMS}I_{RMS}$.

Appendix B. 3D digital image correlation (3D-DIC)

Thirteen sets of 3D DIC experiments defined 3D deformations associated with 6 sets of ERM actuators and 6 sets of C2 tactor actuators at three values of L/L_0 and two values of h_1 and h_2 as well as a single set of LRA actuators at $L/L_0 = 1$ and h_1 as a reference, all on skin phantoms prepared from polydimethylsiloxane, PDMS, (Sylgard 184, Dow Corning) formed with two

different curing agent ratios (30:1 for the top layer and 60:1 for the bottom layer). As an approximation of the epidermis, PDMS at a 30:1 ratio was spin-cast 550 RPM for 60 s on a base slab of PDMS at a 60:1 ratio phantom, to form a layer with thickness around 0.2 mm. The 3D displacements were captured with two high-speed cameras at a sampling rate of 1000 Hz and processed using the open-source 3D DIC software (MultiDIC) [23]. Skin phantom samples were formed for each depth of interest, with surfaces at the corresponding depths uniformly coated with black spray paint (Mehron's water-based face painting) creating speckle patterns with the radius of $\approx 100\text{--}200 \mu\text{m}$ and mean separation of $\approx 600 \mu\text{m}$. The investigation areas were $70 \times 35 \text{ mm}^2$ for ERM actuators and $35 \times 35 \text{ mm}^2$ for tactor actuators. The root mean square error associated with 3D reconstruction was $\sim 50 \mu\text{m}$ for all experiments. To achieve high-resolution, accurate wave-displacement characteristics, the DIC subset radius and spacing were set at 20 and 10 pixels, respectively, resolving over 700 grids.

Appendix C. 3D finite element method

A 3D model with dimension of $100 \text{ mm} \times 100 \text{ mm} \times 20 \text{ mm}$ ($L \times W \times H$) consisted of top and bottom layers with thicknesses of 2 mm and 18 mm, respectively, to match the experimental setup shown in Fig. 1E. The displacement (U) and rotational (R) degrees of freedom were fixed (i.e., $U = R = 0$) for the element nodes at the skin edges and the bottom surface. The element sizes were tested to ensure convergence and accuracy. The total number of elements (C3D8R) was $\sim 125,000$. A total time of 1×10^{-1} s was simulated for both devices with increments of 2.5×10^{-4} s. The instantaneous displacements and strain magnitude contours, calculated over a region of interest of 400 mm^2 , in Figs. 5a and 5b show that the maximum in-plane displacements occur directly underneath the ERM. The out-of-plane displacements show both positive and negative values at the edges. The magnitudes of the displacements gradually decrease with depth. Figs. 5c and 5d show results of similar simulations for the tactor. Unlike the ERM actuator, in this case the maximum in-plane displacements and strains occur at depths beneath the surface. The displacements contours in the in-plane directions shift from positive to negative with depth, due to the change in modulus of the PDMS materials used in the bilayer phantom. For tactor actuator, the maximum out-of-plane displacement occurs at the surface, but the maximum strain occurs at the interface between the top and bottom layers of the phantom, again due to the change in modulus. The PDMS layers in the skin phantom were modeled as Mooney–Rivlin hyper-elastic materials with an elastic modulus (E), Poisson's ratio (ν), and density (ρ) of $E_{\text{skin}} = 50 - 5000 \text{ kPa}$, $\nu_{\text{skin}} = 0.49$, and $\rho_{\text{skin}} = 1116 \text{ kg m}^{-3}$. The vibrotactile sensors were modeled as linear elastic solids with $E_{\text{sensor}} = 113 \text{ GPa}$ and $\nu_{\text{sensor}} = 0.34$, and $\rho_{\text{sensor}} = 8005 \text{ kg m}^{-3}$.

Appendix D. Supplementary data

Supplementary material related to this article can be found online at <https://doi.org/10.1016/j.eml.2022.101940>.

References

- [1] S. Choi, K.J. Kuchenbecker, Vibrotactile display: Perception, technology, and applications, *Proc. IEEE* 101 (9) (2012) 2093–2104.
- [2] Y.H. Jung, J.H. Kim, J.A. Rogers, Skin-integrated vibrohaptic interfaces for virtual and augmented reality, *Adv. Funct. Mater.* 31 (39) (2021) 2008805.
- [3] Y.H. Jung, J.-Y. Yoo, A. Vázquez-Guardado, J.-H. Kim, J.-T. Kim, H. Luan, M. Park, J. Lim, H.-S. Shin, C.-J. Su, A wireless haptic interface for programmable patterns of touch across large areas of the skin, *Nature Electron.* (2022) 1–12.
- [4] M. Kim, S. Lee, S. Choi, Saliency-driven real-time video-to-tactile translation, *IEEE Trans. Haptics* 7 (3) (2013) 394–404.
- [5] A. Cheng, K.A. Nichols, H.M. Weeks, N. Gurari, A.M. Okamura, Conveying the configuration of a virtual human hand using vibrotactile feedback, in: 2012 IEEE Haptics Symposium, HAPTICS, IEEE, 2012, pp. 155–162.
- [6] A. Dementyev, P. Getreuer, D. Kanevsky, M. Slaney, R.F. Lyon, VHP: Vibrotactile haptics platform for on-body applications, in: The 34th Annual ACM Symposium on User Interface Software and Technology, 2021, pp. 598–612.
- [7] B.J. Mortimer, G.A. Zets, R.W. Cholewiak, Vibrotactile transduction and transducers, *J. Acoust. Soc. Am.* 121 (5) (2007) 2970–2977.
- [8] L.A. Jones, A. Singhal, Perceptual dimensions of vibrotactile actuators, in: 2018 IEEE Haptics Symposium, HAPTICS, IEEE, 2018, pp. 307–312.
- [9] M. Azadi, L.A. Jones, Vibrotactile actuators: Effect of load and body site on performance, in: 2014 IEEE Haptics Symposium, HAPTICS, IEEE, 2014, pp. 351–356.
- [10] A. Handler, D.D. Ginty, The mechanosensory neurons of touch and their mechanisms of activation, *Nat. Rev. Neurosci.* 22 (9) (2021) 521–537.
- [11] P. Lamoré, C. Keemink, Evidence for different types of mechanoreceptors from measurements of the psychophysical threshold for vibrations under different stimulation conditions, *J. Acoust. Soc. Am.* 83 (6) (1988) 2339–2351.
- [12] J.C. Makous, G.A. Gescheider, S.J. Bolanowski, The effects of static indentation on vibrotactile threshold, *J. Acoust. Soc. Am.* 99 (5) (1996) 3149–3153.
- [13] T.J. Moore, J.R. Mundie, Measurement of specific mechanical impedance of the skin: Effects of static force, site of stimulation, area of probe, and presence of a surround, *J. Acoust. Soc. Am.* 52 (2B) (1972) 577–584.
- [14] W. McMahan, K.J. Kuchenbecker, Dynamic modeling and control of voice-coil actuators for high-fidelity display of haptic vibrations, in: 2014 IEEE Haptics Symposium, HAPTICS, IEEE, 2014, pp. 115–122.
- [15] R. Hoffmann, V.V. Valgeirsdóttir, Ó.I. Jóhannesson, R. Unnthorsson, Á. Kristjánsson, Measuring relative vibrotactile spatial acuity: Effects of tactor type, anchor points and tactile anisotropy, *Exp. Brain Res.* 236 (12) (2018) 3405–3416.
- [16] R.W. Cholewiak, J.C. Brill, A. Schwab, Vibrotactile localization on the abdomen: Effects of place and space, *Percept. Psychophys.* 66 (6) (2004) 970–987.
- [17] M. Azadi, L.A. Jones, Evaluating vibrotactile dimensions for the design of tactons, *IEEE Trans. Haptics* 7 (1) (2014) 14–23.
- [18] L.M. Brown, S.A. Brewster, H.C. Purchase, A first investigation into the effectiveness of tactons, first joint eurohaptics conference and symposium on haptic interfaces for virtual environment and teleoperator systems, in: World Haptics Conference, IEEE, 2005, pp. 167–176.
- [19] R.D. Gilson, E.S. Redden, L.R. Elliott, Remote Tactile Displays for Future Soldiers, University of Central Florida Orlando, 2007.
- [20] K.O. Sofia, L. Jones, Mechanical and psychophysical studies of surface wave propagation during vibrotactile stimulation, *IEEE Trans. Haptics* 6 (3) (2013) 320–329.
- [21] V.A. Shah, M. Casadio, R.A. Scheidt, L.A. Mrotek, Vibration propagation on the skin of the arm, *Appl. Sci.* 9 (20) (2019) 4329.
- [22] M. Morales-Hurtado, X. Zeng, P. Gonzalez-Rodriguez, J.E. Ten Elshof, E. van der Heide, A new water absorbable mechanical epidermal skin equivalent: The combination of hydrophobic PDMS and hydrophilic PVA hydrogel, *J. Mech. Behav. Biomed. Mater.* 46 (2015) 305–317.
- [23] D. Solav, K.M. Moerman, A.M. Jaeger, K. Genovese, H.M. Herr, MultiDIC: An open-source toolbox for multi-view 3D digital image correlation, *IEEE Access* 6 (2018) 30520–30535.
- [24] A. Kalra, A. Lowe, A. Al-Jumaily, Mechanical behaviour of skin: A review, *J. Mater. Sci. Eng.* 5 (4) (2016) 1000254.
- [25] D. Solav, M. Rubin, A. Wolf, Soft tissue artifact compensation using triangular cosserat point elements (TCPEs), *Internat. J. Engrg. Sci.* 85 (2014) 1–9.
- [26] C. Li, G. Guan, R. Reif, Z. Huang, R.K. Wang, Determining elastic properties of skin by measuring surface waves from an impulse mechanical stimulus using phase-sensitive optical coherence tomography, *J. R. Soc. Interface* 9 (70) (2012) 831–841.